




Article

Variable Stiffness Mechanism for the Reduction of Cutting Forces in Robotic Deburring

Matteo Bottin , Silvio Cocuzza *  and Matteo Massaro 

Department of Industrial Engineering, University of Padova, Via Venezia 1, 35131 Padova, Italy; matteo.bottin@unipd.it (M.B.); matteo.massaro@unipd.it (M.M.)

* Correspondence: silvio.cocuzza@unipd.it; Tel.: +39-049-8276793

Featured Application: The proposed variable stiffness mechanism will be used in robotic deburring applications, in particular in applications with high and irregular burr profiles, ensuring a precision cut without damaging the cutting tool or the robot.

Abstract: One of the main issues related to robotic deburring is that the tool can get damaged or stopped when the burr thickness exceeds a certain threshold. The aim of this work is to devise a mechanism that can reduce cutting forces automatically, in the event that the burr is too high, and is able to return to the baseline configuration when the burr thickness is acceptable again. On the one hand, in normal cutting conditions, the mechanism should have high stiffness to ensure high cutting precision. On the other hand, when the burr is too high the mechanism should exploit its compliance to reduce the cutting forces and, as a consequence, a second cutting cycle will be necessary to completely remove the burr. After the conceptual design of the mechanism and the specification of the desired stiffness curve, the main design parameters of the system are derived thanks to an optimization method. The effectiveness of the proposed mechanism is verified by means of dynamic simulations using selected test cases. A reduction up to 60% of the cutting forces is obtained, considering a steel burr up to 6 mm high.

Keywords: deburring; robot; cutting forces; compliant mechanism



Citation: Bottin, M.; Cocuzza, S.; Massaro, M. Variable Stiffness Mechanism for the Reduction of Cutting Forces in Robotic Deburring. *Appl. Sci.* **2021**, *11*, 2883. <https://doi.org/10.3390/app11062883>

Academic Editor: Giuseppe Carbone

Received: 18 February 2021

Accepted: 18 March 2021

Published: 23 March 2021

Publisher's Note: MDPI stays neutral with regard to jurisdictional claims in published maps and institutional affiliations.



Copyright: © 2021 by the authors. Licensee MDPI, Basel, Switzerland. This article is an open access article distributed under the terms and conditions of the Creative Commons Attribution (CC BY) license (<https://creativecommons.org/licenses/by/4.0/>).

1. Introduction

The deburring process is mainly performed by using manual labor or computerized numerical control (CNC) machines, but in the research field also robotic solutions have been considered [1]. Workers can easily adapt to the unpredictability of the burr, but the dangerous working conditions and the difficulty of the task suggest using dedicated machines. To do so, special CNC machines have been developed, even if a comparable robotic solution costs less than 1/3 than the cost of a CNC machine [2]; moreover, when compared to a CNC machine, an industrial robot can provide a wider workspace, is usually more flexible (since it has a higher number of degrees of freedom), and can provide a higher dexterity, adapting its movement to complex geometries. The drawback of robotic solutions relies on the fact that robots are generally less stiff and accurate than CNC machines [3]: this affects the finishing of the workpiece, can cause chatter [4], and increases the programming and setup time.

The literature related to robotic deburring is limited [1], when compared to the literature related to robotic machining. This can be related to the high variability of the burr profile, which may behave differently depending on the workpiece material [5,6] and may influence burr removal time [7]. In other fields, the effect of burr properties and grinding tool on the final result has been studied. In particular, it has been of great interest in the biomedical field, where the bone grinding is crucial for surgical operations [8]. In fact, the shape of the tool itself provides different deburring results both in terms of temperature

and tool wear [9], which may be fundamental for industrial applications, in which the burr to be removed is made of a material sensible to temperature (e.g., plastics or aluminum) or in intensive and repetitive tasks (e.g., robotic deburring). In depth analysis of the grinding process has been developed for yttrium aluminum garnet (YAG) single crystals, in which it is shown that strain rate plays an important role in the final deformation [10]. This knowledge can be integrated in robotic deburring for specific applications.

In industrial robotics, most of the research effort has focused on obtaining a precise control of the robot motion: Tao et al. [11] developed a sliding mode control method based on radial basis function (RBF) neural network, which is able to learn uncertain control actions. Quian et al. [12] proposed a sensorless force controller that uses the information retrieved only from collaborative robot internal motor sensors to estimate the burr dimensions. Other methods used to handle the high variability of the burr profile include the use of sensors [13,14], but these approaches are not suitable in many deburring applications since the working environment is usually dirty and dusty. If the ambient is clean, however, sensors can be used effectively [15]. El Naser et al. [16] and Gou et al. [17] have developed a robotic arm designed purposely for deburring. This approach is similar to the development of a special CNC machine. On the other hand, Lai et al. [18] have presented a novel design that includes an additional manipulator to be linked to an existing industrial robot. In this way, the kinematic chain becomes similar to the one of a parallel robot, thus increasing stiffness. These last two approaches, however, requires a complex external equipment, which may be expensive and time-consuming for industrial applications.

To increase or decrease the stiffness of the mechanical system during specific tasks, variable stiffness actuators (VSA) and mechanisms have been developed. They can be useful in many fields of application, such as in machining operations, since the stiffness can be changed to improve the surface finishing or reduce vibrations. During the years different solutions have been proposed. Vuong et al. [19] proposed a mechanism that can be tuned to change its stiffness in a wide range, from zero to (theoretically) infinite. It uses multiple linear guides in combination with a moving pivot and linear springs to achieve this functionality. Another example of VSA can be found in [20], in which the authors focused on the compactness of the system and obtained a stiffness inversely proportional to the gear displacement. A variable stiffness robotic arm has also been designed [21]: in this case a 7-degrees-of-freedom manipulator takes advantage of VSA to perform different tasks in the SHERPA mission. Moreover, Petit et al. [22] developed an ad-hoc controller to take advantage of VSA capabilities.

Deburring is a redundant task: the workpiece can be machined on any point of the grinding surface of the grinding wheel. Therefore, it is possible to achieve functional redundancy [23], and the robot can perform the same task using different configurations. For example, if the stiffness and inertial properties of the robot are known or experimentally identified [24,25] it is possible to choose a proper configuration so that the kinematic chain of the robot is stiff enough to perform the grinding operation. However, this field of research has only been partially explored. To overcome the functional redundancy, Nemec et al. [26] proposed to create robot recipes by means of programming by demonstration: by analyzing the movements of an expert human demonstrator, the robot can perform the same task (in this case polishing) exploiting redundancy. Moreover, as can be seen in [27], the stiffness map of a robot can be used to improve the accuracy of the assigned task. In particular, in this work, the authors introduced a compensation strategy to improve a roll hemming process. A stiffness model of a parallel haptic mechanism suitable for real-time computation has been proposed in [28].

When traditional industrial robots are concerned, it is usually difficult to implement force feedback controllers for deburring control purposes. Moreover, industrial applications require high flexibility and reduced implementation costs.

In sum, the literature review suggests that novel deburring techniques are needed to improve flexibility and precision and reduce costs. Indeed, CNC machines provide the

best performance, but are generally more expensive and less flexible when compared to robotic solutions. One of the main issues related to robotic deburring is that the tool can get damaged or stopped when the burr thickness exceeds a certain threshold. A simple system suitable for industrial application is thus required to automatically compensate cutting force peaks. A passive mechanical system is a possible solution: the robot programming remains unaffected, and, if unexpected deburring forces appear, the mechanical system will automatically adapt to reduce the forces applied to the robot.

To achieve this objective, in this paper a simple mechanism is presented that can be used to reduce the peaks of deburring forces that could harm the robot structure or deburring tool. The mechanism will reduce cutting forces automatically if the burr is too high thanks to its compliance, while it will return to the baseline configuration when the burr thickness is acceptable again. The proposed system has also the advantage not to need a high setup time, when compared to a force feedback controller implemented in an industrial robot.

The work is organized as follows: in Section 2 the formulation of deburring forces is covered; in Section 3 the proposed mechanism and its mathematical model are presented; in Section 4 the design of the mechanism is addressed; Section 5 presents the dynamic analysis and simulation of the system in selected test cases; finally, Section 6 concludes the paper.

2. Deburring Forces

Limited information is available about the estimation of deburring forces. However, a simple model has been developed starting from the grinding process [6,29,30]. In the deburring configuration considered (Figure 1), the material is removed by the cylindrical surface of the deburring wheel, with the workpiece moving from the right to the left (along the y axis) and the deburring wheel rotating counterclockwise.

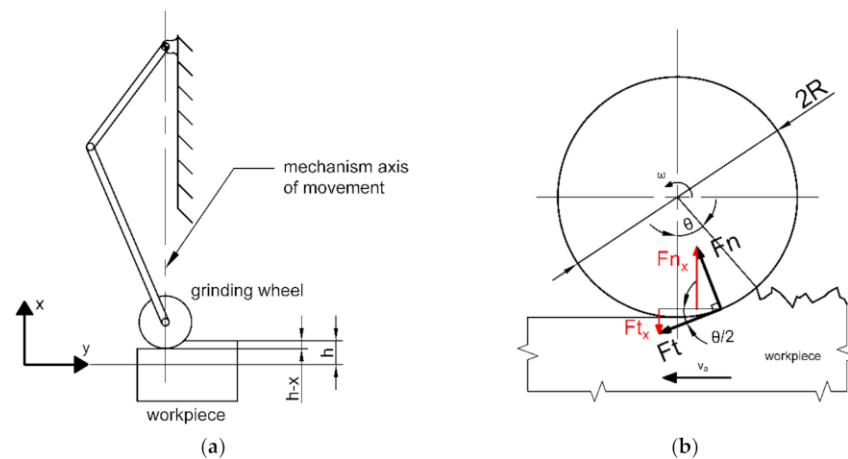


Figure 1. Scheme of the workpiece position in relation to the mechanism axis of movement (a); deburring forces (b).

The material removing rate (MRR) of a single chunk of material can be calculated from the burr dimensions and workpiece movement speed:

$$MRR = b_w \cdot h \cdot v_a \left[\frac{m^3}{s} \right] \quad (1)$$

where b_w and h are the width and height of the material chunk, and v_a is the linear workpiece movement speed. If the material and its specific removal energy u are known

and the rotational speed ω of the grinding wheel is defined, it is possible to calculate the tangential cutting force needed to remove the slice of material as follows:

$$F_t = \frac{b_w \cdot h \cdot v_a \cdot u}{\omega \cdot R} \quad [N] \quad (2)$$

where R is the radius of the grinding wheel.

In practice, (2) depends on the position of the mechanism since the burr height that the grinding wheel removes varies with its x position. As a result, F_t can be expressed as:

$$F_t = \frac{b_w \cdot v_a \cdot u}{\omega} \cdot \frac{(h - x)}{R} \quad (3)$$

It is worthy to point out that the other main force component involved in the cutting process is the force F_n normal to the burr surface. The ratio ($\mu = F_t/F_n$) between F_t and F_n depends on the material, but its value is usually between 0.2 (ceramics and high strength steel) and 0.8 (mild steel) [31]

If the material is removed by a small portion of the grinding wheel surface (Figure 1):

$$h - x = R - R \cos(\theta) \rightarrow \theta = \arccos\left(1 - \frac{h - x}{R}\right) \quad (4)$$

Since F_t and F_n are applied evenly on the surface of the material being removed, it is possible to consider them applied in the middle of the surface, so they are inclined of $\theta/2$ with respect to the y and x axis, respectively. The resulting force along the mechanism x axis is:

$$\begin{aligned} F_{tx} &= F_t \sin\left(\frac{\theta}{2}\right), \quad F_{nx} = F_n \cos\left(\frac{\theta}{2}\right) = \frac{F_t}{\mu} \cos\left(\frac{\theta}{2}\right) \\ F_{tot} &= F_{nx} - F_{tx} = \frac{b_w \cdot v_a \cdot u}{\omega} \cdot \frac{(h - x)}{R} \left(\frac{1}{\mu} \cos\left(\frac{\theta}{2}\right) - \sin\left(\frac{\theta}{2}\right)\right) \end{aligned} \quad (5)$$

It is worth to notice that in practice $R \gg h$, so usually $\theta \rightarrow 0$. Equation (5) is still valid for a generic deburring process, but in this case it is possible to simplify it to calculate the actual normal component of the deburring force applied to the mechanism F_b :

$$F_b \approx \frac{b_w \cdot v_a \cdot u}{\mu \omega} \cdot \frac{(h - x)}{R} \quad (6)$$

3. Proposed Mechanism

It is assumed that the robot arm is holding the workpiece, while the grinding wheel is attached to the ground through the proposed mechanism (Figure 2). The robot end-point trajectory assures the desired depth of cut and feed rate of the piece with respect to the grinding wheel. To develop a mechanism that is as simple as possible, the main compliance direction, assumed normal to the burr (i.e., parallel to the direction of the normal component of the deburring force (6)), should be fixed. The cutting forces that arise during the deburring can be projected along the tangent and normal directions to the burr profile [32], as discussed in Section 2, and the tangential component of the deburring force is balanced by the manipulator.

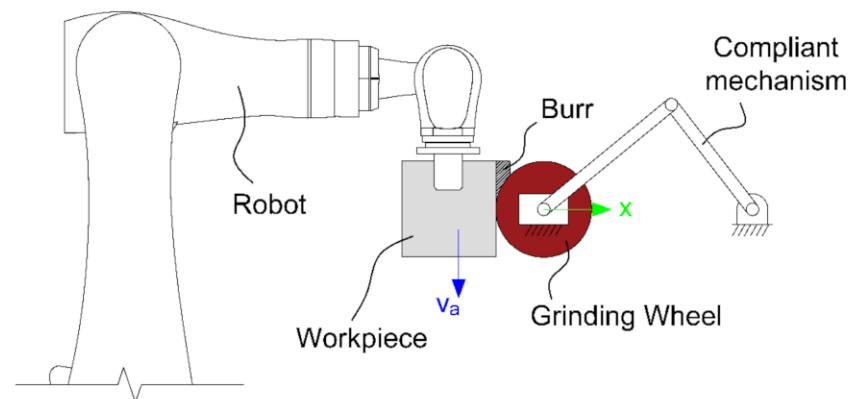


Figure 2. System configuration: the robot holds the workpiece whilst the compliant mechanism holds the grinding wheel.

The main objective is to obtain a mechanism that does not change configuration in normal conditions (assuring a precision cut thanks to its high stiffness), while it changes configuration and reduces its stiffness (and thus the forces applied to the grinding wheel) when the burr exceeds a certain threshold value. In this case, a second cutting cycle is necessary to completely remove the burr.

The proposed mechanism is a slider-crank, where the crank is attached to the ground and the grinding wheel is fixed to the slider. To introduce some forces that allow the system to return to the baseline configuration, some springs are connected to different parts of the mechanism. To obtain a suitable mechanism behavior, it is chosen to place the mechanism close to a singularity, namely close to the top-dead-center (TDC) point. As a result, when the mechanism is close to the TDC, the slider-crank mechanism can react with a maximum force value (see Section 3.1), below which the slider (which supports the grinding wheel) does not move. Of course, if the mechanism is exactly at the TDC, the force value becomes the one giving the structural break of the structure. If this threshold is exceeded, the grinding wheel moves away from the workpiece, thus removing less material, and consequently reducing the cutting force. The slider-crank is ideal for the task at hand since it is easy to build and is suitable for working conditions near the TDC. To avoid to reach the singular configuration, a mechanical stop is applied to the slider (described in more detail in Section 5).

3.1. First Tentative Mechanism

The possibility to add three translational springs to the classic slider-crank mechanism is explored (Figure 3): one for the y -translation of the crank-end (k_1); one for the x -translation of the crank-end (k_2); one for the x -translation of the slider (k_3). In this first stage the springs are connected to sliders, so that their elongations remain parallel to the main axes x and y . The free lengths of the springs are such that they do not generate any forces when the mechanism is in the TDC (angle of the crank $\theta = 0$, and angle of the rocker arm link $\alpha = 0$), i.e., the free length of k_1 is zero, the free length of k_2 is l_1 , while the free length of k_3 depends on the anchor point.

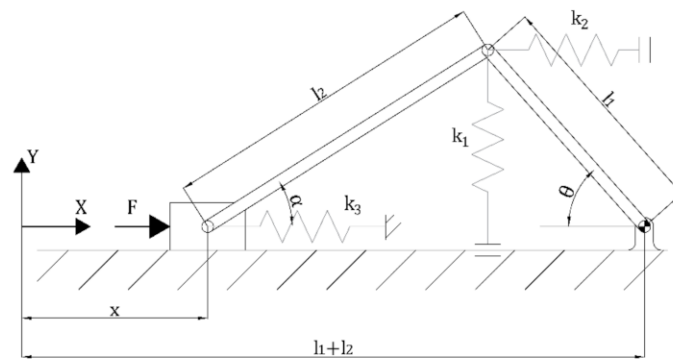


Figure 3. Slider-crank mechanism with three translational springs, two of which are connected to sliders so that their movement is purely along one axis. l_1 is the crank length, l_2 is the rocker arm link length.

When neglecting friction forces, the principle of virtual work gives:

$$\delta L = 0 \rightarrow \sum_i \delta L_i = \sum_i F_i \cdot \delta x_i = 0 \quad (7)$$

where F_i is the i -th force applied to the mechanism, δx_i is the associated virtual displacement, and δL_i the related virtual work. From the mechanism configuration of Figure 3 and (7) it is found that:

$$F \cdot \delta x - k_3 x \cdot \delta x - k_1 s_1 \cdot \delta s_1 - k_2 s_2 \cdot \delta s_2 = 0 \quad (8)$$

where:

$$\begin{aligned} s_1 &= l_1 \sin \theta \rightarrow \delta s_1 = l_1 \cos \theta \cdot \delta \theta \\ s_2 &= l_1 (1 - \cos \theta) \rightarrow \delta s_2 = l_1 \sin \theta \cdot \delta \theta \end{aligned} \quad (9)$$

Substituting s_1 , s_2 , and their differentials in (8) results in:

$$(F - k_3 x) \delta x - (k_1 l_1^2 \sin \theta \cos \theta + k_2 l_1^2 (1 - \cos \theta) \sin \theta) \delta \theta = 0 \quad (10)$$

It is possible to calculate the magnitude of the force F that is balanced by the springs in each configuration of the mechanism starting from the speed ratios of the slider-crank mechanism:

$$\tau_{\theta x} = \frac{\dot{\theta}}{\dot{x}} = \frac{\cos(\alpha)}{l_1 \sin(\alpha + \theta)} = \frac{\delta \theta}{\delta x}, \quad \tau_{\alpha x} = \frac{\dot{\alpha}}{\dot{x}} = \frac{\cos(\theta)}{l_1 \sin(\alpha + \theta)} = \frac{\delta \alpha}{\delta x} \quad (11)$$

and using them in (10), which results in:

$$F = k_3 x + \frac{k_1 l_1 \sin \theta \cos \theta \cos \alpha + k_2 l_1 (1 - \cos \theta) \sin \theta \cos \alpha}{\sin(\alpha + \theta)} \quad (12)$$

This equation is only a function of the variable x , since α and θ can be written as:

$$\begin{aligned} \theta &= \arccos\left(\frac{l_1^2 + (l_1 + l_2 - x)^2 - l_2^2}{2l_1(l_1 + l_2 - x)}\right) \\ \alpha &= \arcsin\left(\frac{l_1}{l_2} \sin \theta\right) \end{aligned} \quad (13)$$

Starting from (12) it is possible to obtain different behaviors of the mechanism by changing the stiffnesses of springs and link lengths. As an example, in Figure 4 two configurations are shown: to the left only the springs k_1 and k_2 are used, while to the right only k_1 and k_3 are used. In the first case the mechanism can withstand higher forces with the increase of x , whereas in the second case the opposite happens.

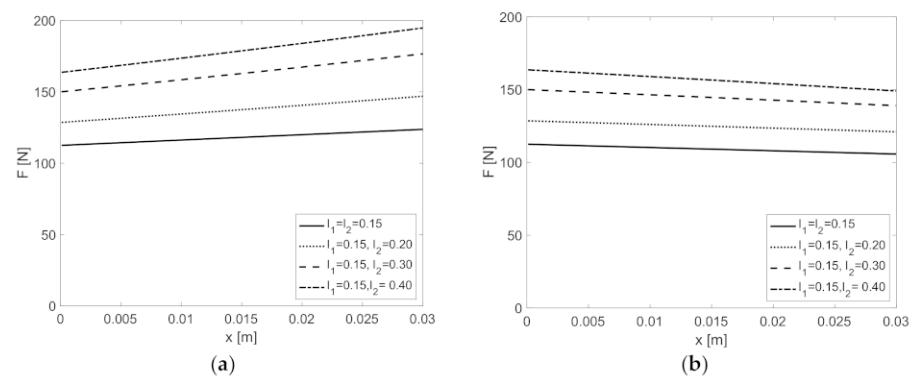


Figure 4. Variation of the force necessary to maintain the mechanism in static equilibrium as a function of x . (a) Only k_1 and k_2 are used ($k_1 = 1500$ N/m, $k_2 = 3000$ N/m). (b) Only k_1 and k_3 are used ($k_1 = 1500$ N/m, $k_3 = 150$ N/m).

It is important to notice that the force F results in a finite value when the mechanism is close to the TDC configuration, and this force is a function of k_1 only, i.e., (12) when $x \rightarrow 0$ and using (13) becomes:

$$\lim_{x \rightarrow 0} F = k_1 \frac{l_1 l_2}{l_1 + l_2} \quad (14)$$

In sum, both progressive and regressive forces as a function of the slider displacement can be obtained with the proposed mechanism and layout, together with a finite value force for configurations close to the TDC. These last two are precisely the ingredients necessary to build a system capable of reducing the cutting forces when the deburring height exceeds a given threshold. Indeed, during deburring the grinding wheel has to remove a certain amount of material, while preserving the structural integrity of the robot. The mechanism is able to withstand a certain deburring force (finite value around the TDC). When this threshold is exceeded, the mechanism becomes compliant (with regressive curve), thus reducing the cutting forces.

3.2. Final Mechanism

The mechanism proposed in Section 3.1, although theoretically suitable for the target application, is difficult to build. In particular, it would be quite impractical to include sliders at the anchor points with the frame, in order to keep the springs aligned with the reference axes. Therefore, a new mechanism is proposed with the springs fixed at some distance from the crank fixed hinge (Figure 5). Even with this modification, the basic principles described in Section 3.1 hold valid.

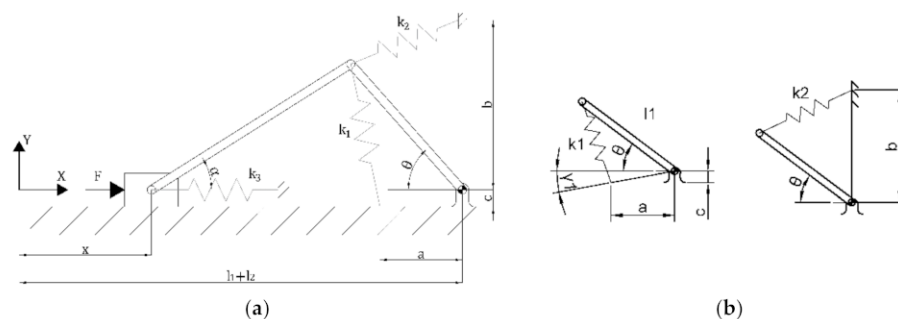


Figure 5. Slider-crank mechanism with translational springs connected to fixed ends (a). Two particulars of the mechanism are shown in the right figure (b).

Additionally, in this modified design, the springs are unloaded when the mechanism is close to the TDC ($x \rightarrow 0$). The principle of virtual work is to be applied in the same way as in (7), but the virtual displacements of k_1 and k_2 (s_1 and s_2 , respectively) have to be

modified according to the new mechanism. Starting from the dimensions of Figure 5, the spring displacements are:

$$\begin{aligned}s_1 &= \sqrt{l_1^2 + d^2 - 2l_1d \cos(\gamma_1 + \theta)} - \sqrt{(a - l_1)^2 + c^2} \\s_2 &= \sqrt{l_1^2 + b^2} - \sqrt{l_1^2 + b^2 - 2l_1b \sin(\theta)}\end{aligned}\quad (15)$$

where d is the distance between the anchor point of k_1 and the crank hinge, and γ_1 is the angle of the vector crank hinge-anchor point with respect to the x -axis:

$$d = \sqrt{a^2 + c^2}, \quad \gamma_1 = \text{atan}\left(\frac{c}{a}\right) \quad (16)$$

The differentials of s_1 and s_2 can be calculated as:

$$\begin{aligned}\delta s_1 &= \frac{\partial s_1}{\partial \theta} \cdot \delta \theta = \frac{l_1 d \sin(\gamma_1 + \theta)}{\sqrt{l_1^2 + d^2 - 2l_1d \cos(\gamma_1 + \theta)}} \cdot \delta \theta \\ \delta s_2 &= \frac{\partial s_2}{\partial \theta} \cdot \delta \theta = \frac{l_1 b \cos(\theta)}{\sqrt{l_1^2 + b^2 - 2l_1b \sin(\theta)}} \cdot \delta \theta\end{aligned}\quad (17)$$

As a result, the force F at the slider becomes:

$$F = k_3 x + \left(k_1 s_1 \frac{l_1 d \sin(\gamma_1 + \theta)}{\sqrt{l_1^2 + d^2 - 2l_1d \cos(\gamma_1 + \theta)}} + k_2 s_2 \frac{l_1 b \cos(\theta)}{\sqrt{l_1^2 + b^2 - 2l_1b \sin(\theta)}} \right) \tau_{\theta x} \quad (18)$$

The expression (18) for $x \rightarrow 0$ simplifies to:

$$\lim_{x \rightarrow 0} F = \frac{k_1 l_1 l_2 c^2 (b^2 + l_1^2) + k_2 l_1 l_2 b^2 ((a - l_1)^2 + c^2)}{(l_1 + l_2) ((a - l_1)^2 + c^2) (b^2 + l_1^2)} \quad (19)$$

Differently from (14), which depends on k_1 only, (19) depends both on k_1 and k_2 . Similarly to the mechanism of Figure 3, the new mechanism behaviour depends on its main dimensions. Nevertheless, in this case also the dimensions a , b , and c have a great impact on F . As an example, two different mechanisms are shown in Figure 6, whose main parameters are listed in Table 1. Similarly to the mechanism presented in Section 3.1., both progressive and regressive forces as a function of the x displacement can be obtained, with a finite value of the force around the TDC. The regressive curve is preferred for the application at hand since it is related to lower cutting forces.

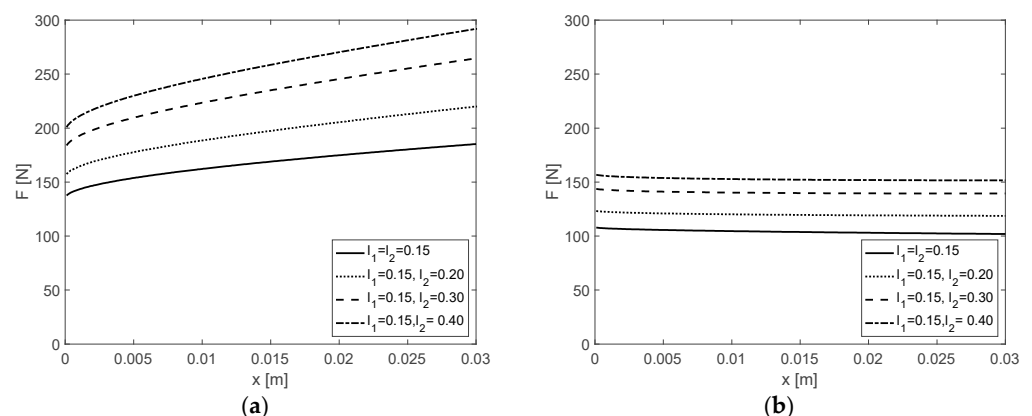


Figure 6. Variation of the force necessary to maintain the mechanism in static equilibrium as a function of x . ((a) Mechanism #1, (b) Mechanism #2).

Table 1. Main mechanism parameters.

Parameter	Mechanism #1	Mechanism #2
l_1	0.15 m	
l_2	[0.15, 0.2, 0.3, 0.4] m	
a	0.05 m	0.14 m
b	0.15 m	0.03 m
c	0.05 m	
k_1	1500 N/m	
k_2	3000 N/m	0
k_3	200 N/m	0

4. Design

In normal cutting conditions, the mechanism should have high stiffness to ensure high cutting precision. On the other hand, when the burr is too high the mechanism should exploit its compliance to reduce the cutting forces and, as a consequence, a second cutting cycle is necessary to completely remove the burr.

The desired regressive behavior of the mechanism is related to its geometrical parameters and to the springs stiffness. If the link lengths (l_1 and l_2) are defined by the scale of the application (related to the workpiece dimensions and maximum burr height), there are 5 other parameters to be chosen (see Figure 5): k_1 , k_2 , k_3 , a , and b . It is not straightforward to find a good set of values by trial-and-error, so an optimization algorithm has been used. The algorithm aims at finding the parameters whose resulting mechanism forces F fit a desired (regressive) curve.

In this work the desired force profile is set to $F = 150 - 300x$ [N] (blue dotted line in Figure 7) with $l_1 = 0.15$ m and $l_2 = 0.3$ m. The *fmincon* MATLAB function has been used to find the optimal parameters that minimize the error between the actual and desired force profiles. The optimization algorithm yields the values listed in Table 2. It is worth to notice from Figure 7 that the system is stable: the normal component of the deburring force (F_b) decreases with x faster than the elastic force on the slider (F):

$$\frac{\partial F_b}{\partial x} < \frac{\partial F}{\partial x} \quad (20)$$

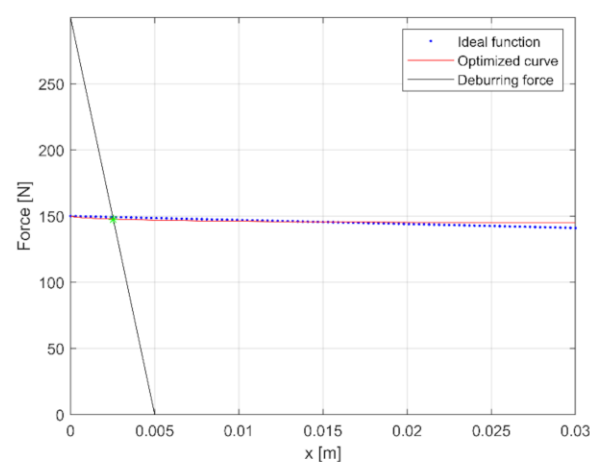


Figure 7. The optimization algorithm finds the mechanism parameters whose $F(x)$ (red line) fits at best the objective curve (blue dotted line). Black line shows how $F_b(x)$ decreases with the movement of the mechanism (with $h = 5$ mm).

Table 2. Parameters computed by the optimization algorithm.

k_1	k_2	k_3	a	b
1560 N/m	47 N/m	≈ 0 N/m	0.14 m	0.028 m

The black line of Figure 7 is the deburring force (normal component, as discussed in Section 2). This curve moves to the right for higher burr heights (with higher cutting forces for $x = 0$), and vice versa. The intersection between this line and the optimized curve (red line in figure) yields the equilibrium point, i.e., the x value at which the mechanism moves to balance the deburring force and the elastic force of the mechanism. For very low values of h the black line does not intersect the optimized curve, so the mechanism does not move. In this case, a precision cut is ensured, with cutting forces below the force threshold that activates the mechanism compliance. For the parameters of Table 2 and Figure 7 (see Table 3 in Section 5.3 for the complete list of parameters) the burr height (steel) that activates the mechanism compliance is 2.5 mm.

Table 3. Simulation parameters.

Parameter	Value
b_w	$1 * 10^{-3}$ m
v_a	$15 * 10^{-3}$ m/s
u (steel)	$30 * 10^9$ J/m ³
ω	100 rad/s
R	0.1 m
μ	0.75
c_{eq}	2000 Ns/m
k_1	1560 N/m
k_2	47 N/m
k_3	0 N/m
a	0.14 m
b	0.028 m
c	0.05 m
l_1	0.15 m
l_2	0.3 m
m	30 kg
m_r	1.0 kg
m_c	0.5 kg
k_{stop}	10^7 N/m
$x_{stop} = x_0$	$3 * 10^{-4}$ m
x_1	0 m
h_0	0 Ns/m
h_1	10^4 Ns/m

It is important to notice that it is possible to perform the optimization starting from a different desired force curve and, in particular, different force thresholds can be set depending on the application. This will result in a different set of springs and anchor points.

From a mechanical point of view, it is important to include a mechanical end stop for the slider to avoid possible changes in configuration of the slider-crank (i.e., to keep the rocker arm link always above the slider axis) and to avoid that the mechanism works in the TDC. Indeed, the mechanism is designed to work near the TDC, where it can generate a finite elastic force, but not exactly in the TDC, which could be dangerous for the structural integrity of the mechanism if the burr height is very large. The detailed model of the end stop will be presented in Section 5.2.

5. Dynamic Analysis

5.1. Dynamic Model

The proposed mechanism has one degree of freedom and can thus be modeled using a single equivalent mass m^* that is excited via a single equivalent force F^* . The equivalent mass and force clearly depend on the mechanism configuration (x) and on its main parameters.

The equations of motion are obtained by recalling that the power equals the derivative of the kinetic energy:

$$P = \frac{dE_k}{dt} \quad (21)$$

Since friction between the members of the mechanism and their potential energy can be neglected. The kinetic energy of the equivalent mass equals by definition the kinetic energy of all the members of the mechanism:

$$E_k = \frac{1}{2}m^*\dot{x}^2 = \frac{1}{2}\left(m\dot{x}^2 + m_r(\dot{x}_{Gr}^2 + \dot{y}_{Gr}^2) + I_r\dot{\alpha}^2 + m_c(\dot{x}_{Gc}^2 + \dot{y}_{Gc}^2) + I_c\dot{\theta}^2\right) \quad (22)$$

where \dot{x} is the velocity of the equivalent mass (equal to the one of the slider); m is the mass of the slider (included the spindle and the grinding wheel); m_r , I_r , \dot{x}_{Gr} , \dot{y}_{Gr} are the mass, barycentric moment of inertia, barycenter velocity along the x axis, and barycenter velocity along the y axis of the rocker arm link, respectively; m_c , I_c , \dot{x}_{Gc} , \dot{y}_{Gc} are the mass, barycentric moment of inertia, barycenter velocity along the x axis, and barycenter velocity along the y axis of the crank, respectively. The coordinates of the centers of mass of the rocker arm link and of the crank are (respectively):

$$\begin{Bmatrix} x_{Gr} \\ y_{Gr} \end{Bmatrix} = \begin{Bmatrix} x + \frac{l_2}{2}\cos(\alpha) \\ \frac{l_2}{2}\sin(\alpha) \end{Bmatrix}, \quad \begin{Bmatrix} x_{Gc} \\ y_{Gc} \end{Bmatrix} = \begin{Bmatrix} l_1 + l_2 - \frac{l_1}{2}\cos(\theta) \\ \frac{l_1}{2}\sin(\theta) \end{Bmatrix} \quad (23)$$

The corresponding velocities are:

$$\begin{Bmatrix} \dot{x}_{Gr} \\ \dot{y}_{Gr} \end{Bmatrix} = \begin{Bmatrix} \dot{x} - \frac{l_2}{2}\sin(\alpha)\dot{\alpha} \\ \frac{l_2}{2}\cos(\alpha)\dot{\alpha} \end{Bmatrix}, \quad \begin{Bmatrix} \dot{x}_{Gc} \\ \dot{y}_{Gc} \end{Bmatrix} = \begin{Bmatrix} \frac{l_1}{2}\sin(\theta)\dot{\theta} \\ \frac{l_1}{2}\cos(\theta)\dot{\theta} \end{Bmatrix} \quad (24)$$

By introducing (24) and the speed ratios of (11), the final form of (22) is:

$$\frac{1}{2}m^*\dot{x}^2 = \frac{1}{2}\left(m + m_r\left(1 + \frac{l_2^2}{4}\tau_{\alpha x}^2 - l_2\sin(\alpha)\tau_{\alpha x}\right) + I_r\tau_{\alpha x}^2 + m_c\left(\frac{l_1^2}{4}\tau_{\theta x}^2 + I_c\tau_{\theta x}^2\right)\dot{x}^2\right) \quad (25)$$

The power P of F^* can be calculated from the deburring force and the springs forces:

$$P = F^*\dot{x} = -(k_1s_1)\dot{s}_1 - (k_2s_2)\dot{s}_2 - (k_3x)\dot{x} - (c_{eq}\dot{x})\dot{x} + F_b\dot{x} \quad (26)$$

in which the force of a damper to be connected in parallel to spring k_3 (with damping c_{eq}) is introduced in order to avoid undesired vibrations.

The equation of motion is found by differentiating (25) and putting it equal to (26):

$$m^*\ddot{x} + \frac{1}{2}\left(\left(2I_r + \frac{l_2^2}{2}m_r\right)\tau_{\alpha x}\dot{\tau}_{\alpha x} + \left(2I_c + \frac{l_1^2}{2}m_c\right)\tau_{\theta x}\dot{\tau}_{\theta x} - m_rl_2(\tau_{\alpha x}\dot{\alpha}\cos(\alpha) + \dot{\tau}_{\alpha x}\sin(\alpha))\right)\dot{x}^2 = F^*\dot{x} \quad (27)$$

The differential Equation (27) is implemented and solved numerically in MATLAB for different working scenarios. The simulation results and the simulation parameters used are presented in Section 5.

5.2. Mechanical Stop Model

To avoid the singular configuration at the TDC and changes in the mechanism configuration, a mechanical stop has been introduced. The mechanical stop should be made of soft material to reduce unnecessary shocks to the mechanism structure. The mechanical stop is modeled as a one degree of freedom system that is activated as soon as $x_{sup} < x_{stop}$, in which x_{sup} is the coordinate of the surface of the slider and x_{stop} is the coordinate of the mechanical stop when the slider is not in contact with it (see Figure 8).

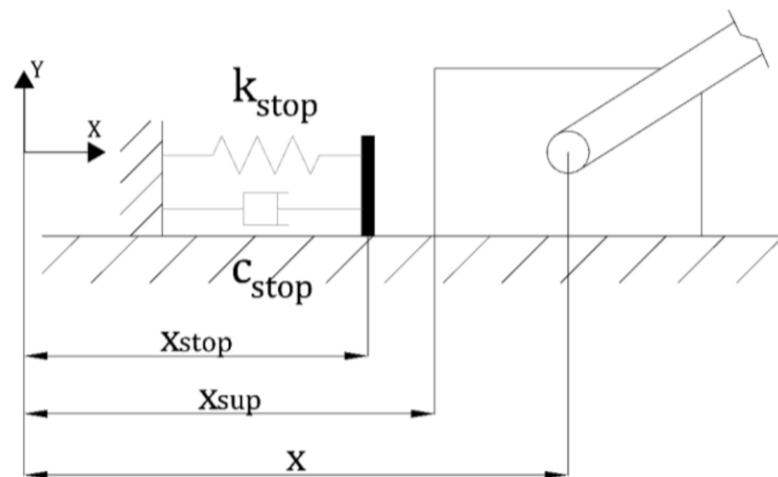


Figure 8. Model of the mechanical stop of the mechanism.

The force transferred by the mechanical stop to the mechanism is:

$$F_{stop} = k_{stop}(x_{sup} - x_0)^e + f(x_{sup}, x_0, h_0, x_1, h_1)\dot{x} \quad (28)$$

where:

- k_{stop} is the stiffness of the mechanical stop;
- x_{sup} is the coordinate of the surface of the slider that impacts the mechanical stop;
- $x_0 (=x_{stop})$ and x_1 are the coordinates of the limits of the mechanical stop;
- e is the exponent in (28), which is null in the case of the Kelvin-Voigt model;
- h_0 and h_1 are the limits of the function f .

Function f is described by a polynomial function, whose normalized shape is shown in Figure 9:

$$f(x_{sup}, x_0, h_0, x_1, h_1) = \begin{cases} h_0 & x_{sup} \geq x_0 \\ h_0 + a\Delta^2(3 - 2\Delta) & x_1 \leq x_{sup} \leq x_0 \\ h_1 & x_{sup} \leq x_1 \end{cases} \quad (29)$$

where:

$$a = h_1 - h_0, \quad \Delta = \frac{x_{sup} - x_0}{x_1 - x_0} \quad (30)$$

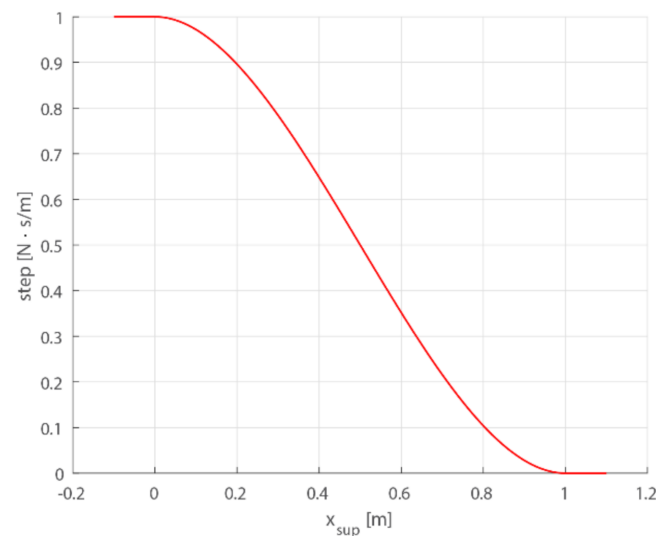


Figure 9. Normalized shape of function f (29).

5.3. Simulation Results

In this section the results of the dynamic simulations of the proposed system in different working conditions are presented. The main aim of the simulations is to verify that the mechanism works properly and, in particular, it is important to check the following conditions:

1. If the projection of the cutting force along the sliding direction is less than the elastic force threshold of the mechanism, then the grinding wheel support should not move. This happens for small burr heights. With the considered setup (specified in Table 3), the elastic force threshold of the mechanism, which is equal to the elastic reaction force for $x \rightarrow 0$, is 149.01 N. This force threshold corresponds to a burr height of 2.5 mm with the considered setup.
2. If the projection of the cutting force along the sliding direction exceeds the elastic force threshold, the grinding wheel support should move backwards according to the compliance of the mechanism and the dynamics of (27); moreover, for a constant burr height, an equilibrium condition should be achieved (after a transient) between the cutting force projection and the elastic reaction force and, therefore, a cut profile with constant height should be obtained.
3. If the burr height decreases, the compliant mechanism should move forward, and return towards the TDC. This condition is very important since it assures the stability of the system. Of course, even if the burr becomes very small, the mechanism can never reach the TDC due to the mechanical stop.

Condition 1 assures the cutting precision of the system, if the cutting force (and the burr height) is below a given threshold. Condition 2 assures that the mechanism is compliant if the cutting forces are too high, so that they are reduced to an acceptable value; nevertheless, the cutting precision is jeopardized and an additional cutting cycle is necessary to completely remove the burr. Condition 3 assures that the mechanism returns back (up to the initial configuration) if the burr height decreases.

In the simulations the parameters listed in Table 3 are used. A steel burr is considered with $\mu = 0.75$ [31]. The mechanical stop has been modeled as discussed in Section 5.2.

Different burr profiles are used as an input to simulations. The outputs of simulations are the position x (directly related to the cut profile) and velocity \dot{x} of the grinding wheel support as a function of time. In order to verify the conditions 1–3, simulations are carried out with step variations of burr height. Between different steps the burr height is constant in order to verify that an equilibrium condition (cut profile with constant height) is obtained after an initial transient. Different test cases with different profiles of step burr height

are analyzed as detailed below (Sections 5.3.1–5.3.5). Finally, this study will include a simulation in which the burr height is defined by a random function (Section 5.3.6).

The dynamic simulations start (for $t = 0$ s) with the grinding wheel support in contact with the mechanical stop. For this reason, the position x is 0.3 mm for $t = 0$ s in all the simulations performed, which corresponds to the position of the mechanical stop. This means that the mechanism initial configuration is very near to the TDC. Due to the initial length of the springs, a small elastic force is present that presses the grinding wheel support against the mechanical stop.

5.3.1. Test Case 1—1-Step Profile

A 1-step burr profile with a constant height ($h = 5$ mm, see solid line in Figure 10 (top)) is used as an input for the dynamic simulation. The burr height is sufficiently high to make the projection of the cutting force along the sliding direction exceed the elastic force threshold of the mechanism (dashed line in Figure 10). The simulation results, i.e., the position and velocity of the grinding wheel support in function of time, are presented in Figure 10 (middle and bottom). From the analysis of Figure 10, it can be noticed that the grinding wheel support moves backwards (positive values of x) thanks to the compliance of the mechanism; moreover, an equilibrium condition is achieved (after a transient of about 0.25 s with a small overshoot) between the cutting force projection and the elastic reaction force and, therefore, a cut profile with constant height is obtained. Therefore, the simulation results for this test case are in line with what was expected in this case (Condition 2 of Section 5.3). The burr height, initially equal to 5 mm, after processing is about 2.5 mm. This means that a second cutting cycle is necessary to completely remove the burr. The maximum (normal) deburring force reduces to 148 N from the nominal value of 300 N (corresponding to the nominal height of 5 mm), i.e., roughly a 50% (automatic) force reduction is obtained, which is related to the 50% reduction of the cutting height (2.5 instead of 5 mm).

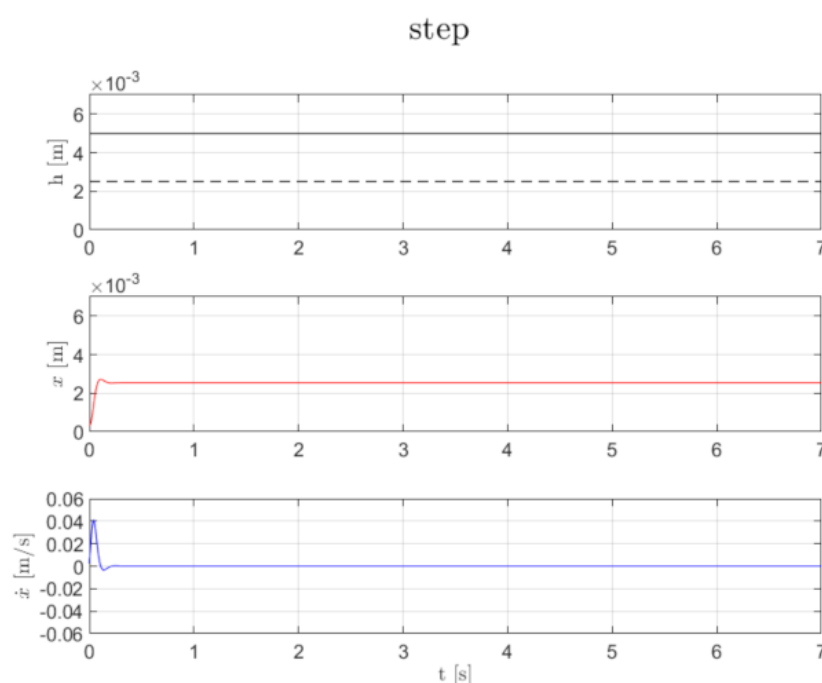


Figure 10. Step burr profile ($h = 5$ mm, **top**); position (**middle**) and velocity (**bottom**) of the grinding wheel support.

5.3.2. Test Case 2—3-Steps Burr Profile “Low–Low–High”

A 3-steps burr profile “low–low–high” (see Figure 11 (top)) is used as an input for the dynamic simulation. “Low”/“high” means that the burr height is not/is sufficiently high

to make the projection of the cutting force along the sliding direction exceed the elastic force threshold of the mechanism. In this test case, steps with increasing height are investigated. In the first two steps the cutting force is below the elastic force threshold, whereas in the third step the cutting force is sufficiently high (above the threshold) to make the mechanism work in the compliant mode of operation. The simulation results are presented in Figure 11 (middle and bottom). It can be noticed that the grinding wheel support does not move while the first two steps are processed (precision cut), and it moves backwards thanks to the compliance of the mechanism while the third step is processed. Similarly to the previous test case, an equilibrium condition is achieved (after a transient of about 0.3 s after the beginning of step 3) and a cut profile with constant height is obtained for step 3, as it can be noticed in Figure 11. Additionally, in this test case the simulation results confirm the expected dynamic behavior of the system: the grinding wheel support moves backward only when the cutting force projection exceeds the elastic force threshold, and when this happens a constant cut profile is obtained, after an initial transient (Condition 1 and Condition 2 of Section 5.3). From another point of view, for small burr heights the mechanism is (ideally) infinitely stiff, whereas it becomes compliant for high burr heights. Some small oscillations can be noticed when the burr height changes value but is not sufficiently high to allow the mechanism to work in the compliant mode (i.e., the grinding wheel support does not move and the cutting precision is ensured). This is due to the presence of the mechanical stop, which is not infinitely stiff. Nevertheless, this effect causes a negligible effect on the grinding wheel position, as it can be noticed in Figure 11 (middle). The maximum (normal) deburring force reduces again to 148 N from the nominal value of 240 N (corresponding to the nominal height of 4 mm), i.e., roughly a 38% (automatic) force reduction is obtained, which is related to the 38% reduction of the cutting height (2.5 instead of 4 mm).

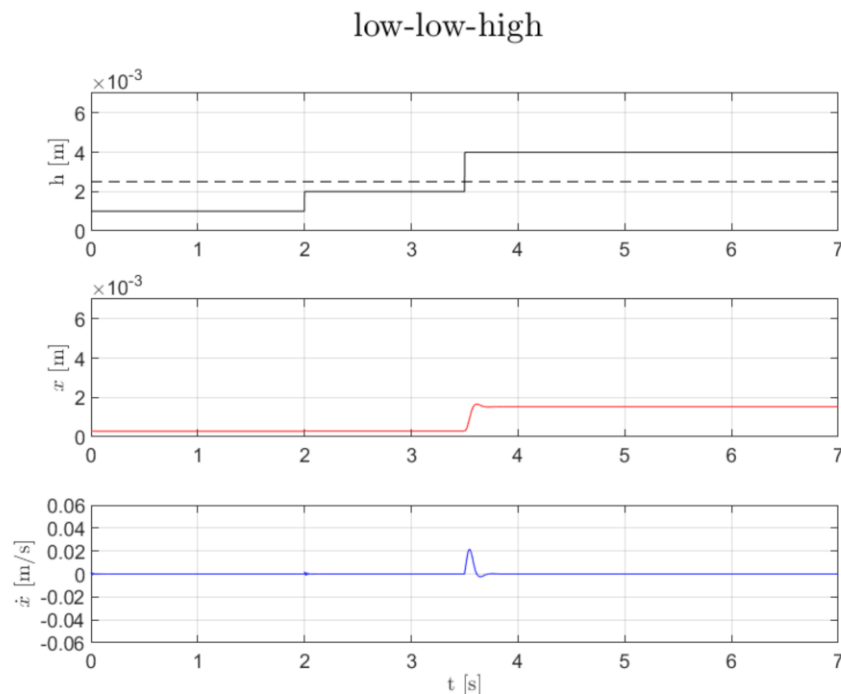


Figure 11. Three-steps burr profile (“low–low–high” (**top**)); position (**middle**) and velocity (**bottom**) of the grinding wheel support.

5.3.3. Test Case 3—3-Steps Burr Profile “High–High–High”

A 3-steps burr profile “high–high–high” (see Figure 12 (top)) is used as an input for the dynamic simulation. Similarly to the previous test case, 3 steps with increasing height are investigated. Differently with respect to the previous test case, in this case, for all the 3

steps the cutting force is sufficiently high to make the mechanism work in the compliant mode of operation. The aim of this test case is to verify that, when it passes from one step to another, the system moves from an equilibrium condition to a new equilibrium condition. The simulation results are presented in Figure 12 (middle and bottom). It can be noticed that, at each step, the grinding wheel moves backwards thanks to the compliance of the mechanism. Three different equilibrium conditions are achieved (after a transient of about 0.25 s each time) with increasing height of the residual burr and, inside each step, a cut profile with constant height is obtained (after the transient), as it can be noticed in Figure 12. The simulation results of this test case confirm the expected dynamic behavior of the system: each time that the system encounters a higher step, it moves to a new equilibrium condition with a higher height of residual burr (in particular, Condition 2 of Section 5.3 is satisfied for all the 3 steps). The maximum (normal) deburring force reduces to 147.3 N from the nominal value of 360 N (corresponding to the nominal height of 6 mm), i.e., roughly a 60% (automatic) force reduction is obtained, which is related to the 60% reduction of the cutting height (2.5 instead of 6 mm).

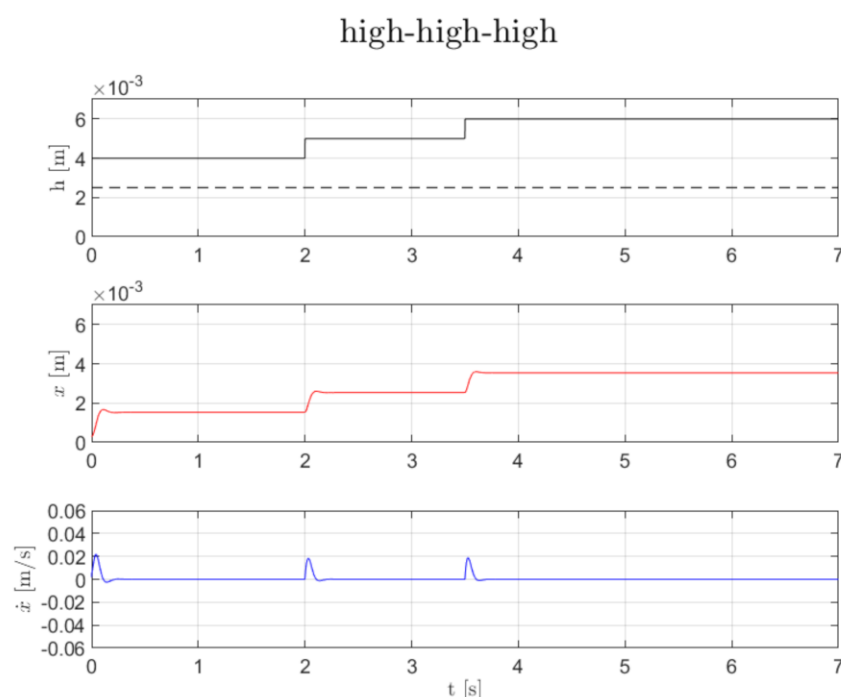


Figure 12. Three-steps burr profile (“high-high-high” (top)); position (middle) and velocity (bottom) of the grinding wheel support.

5.3.4. Test Case 4—3-Steps Burr Profile “High-Highest-High”

A 3-steps burr profile “high-highest-high” (see Figure 13 (top)) is used as an input for the dynamic simulation. The burr height is $h = 4$ mm in the first step, then it becomes $h = 6$ mm in the second step, and finally it returns to $h = 4$ mm in the third step. In all the three steps the burr height is sufficiently high to make the mechanism work in the compliant mode of operation. The main aim of this test case is to verify that, if the burr height decreases, the compliant mechanism moves forward and returns towards the TDC, as specified in Condition 3 of Section 5.3. The simulation results are presented in Figure 13 (middle and bottom). It can be noticed that, during the first two steps, the grinding wheel moves backwards thanks to the compliance of the mechanism, and two different equilibrium conditions are achieved with increasing height of the residual burr. Moreover, in the third step, the compliant mechanism moves forward and rapidly returns towards the TDC. In this step, a new equilibrium condition is obtained, with the same height of residual

burr as in the step 1 (as expected, since the burr height is equal in steps 1 and 3). Therefore, the mechanism works properly and, in particular, Condition 3 of Section 5.3 is satisfied.

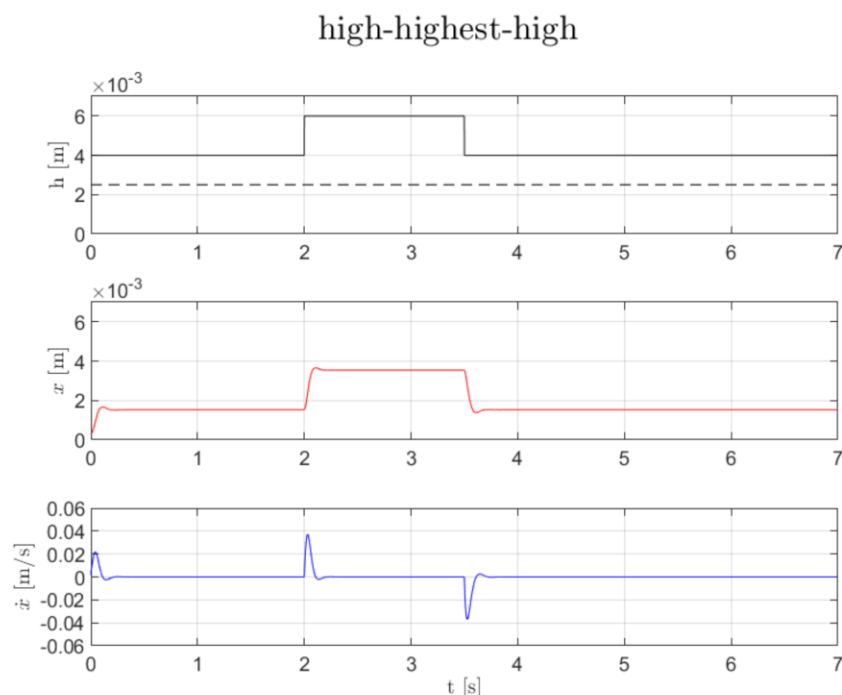


Figure 13. Three-steps burr profile (“high–highest–high” (top)); position (middle) and velocity (bottom) of the grinding wheel support.

5.3.5. Test Case 5—3-Steps Burr Profile “High–Low–High”

A 3-steps burr profile “high–low–high” (see Figure 14 (top)) is used as an input for the dynamic simulation. In the first and third step the burr height is sufficiently high to make the mechanism work in the compliant mode of operation, whereas in the second step the burr height is sufficiently low to generate a cutting force projection below the elastic force threshold. The main aim of this test case is to verify that, when the burr height decreases and generates a cutting force projection below the elastic force threshold, the mechanism returns in the initial configuration, i.e., with the grinding wheel support in contact with the mechanical stop. The simulation results are presented in Figure 14 (middle and bottom). It can be noticed that, during the first step, the grinding wheel moves backwards thanks to the compliance of the mechanism, and an equilibrium condition is achieved with a certain height of the residual burr. In the second step, the compliant mechanism moves forward and rapidly returns towards the TDC (Condition 3 of Section 5.3 is satisfied). Since the cutting force projection is below the elastic force threshold, the mechanism would tend to go to the TDC, but due the mechanical stop this is not possible. Indeed, an impact between the grinding wheel support and the mechanical stop takes place, as it can be noticed in Figure 14, in which small bounces are reported after $t = 1.5$ s. Of course, the amplitude and damping of these bounces depend on the dynamic parameters of the mechanism (masses, inertias, springs stiffness, and damping) and on the characteristics (stiffness and damping) of the mechanical stop. After the bounces, the mechanism remains in the initial configuration (x is about 0.3 mm, as it can be noticed in Figure 14), up to the beginning of the third step. Finally, in the third step, a new equilibrium condition is obtained, with a height of residual burr higher than in the first step (as expected, since the burr height is higher).

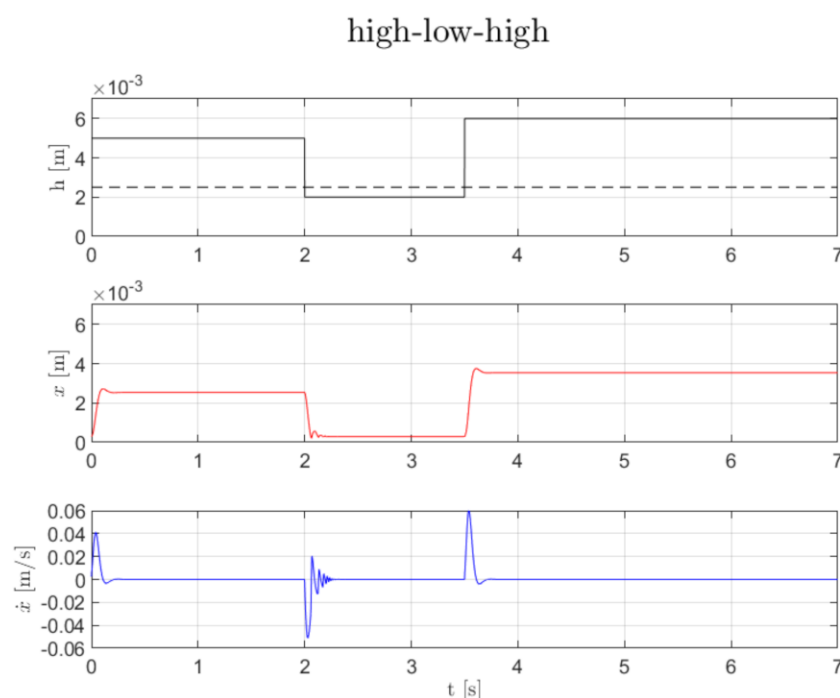


Figure 14. Three-steps burr profile (“high–low–high” (top)); position (middle) and velocity (bottom) of the grinding wheel support.

5.3.6. Test Case 6—Generic Burr Profile

A set of generic burr profiles have been generated using a random variation of burr height in order to test the mechanism in more realistic scenarios. The random burr profiles are then used as an input for the dynamic simulations. Random profiles have been generated starting from the power spectral density (PSD) of the random process [33]. The three most common shapes for the noise have been assumed, namely white noise (flat PSD), flicker-noise (PSD with slope -1 in a log-log diagram), and random-walk noise (PSD with slope-2). The latter is usually adopted when it comes to the roughness of road surfaces (ISO 8608:2016). The shape of the PSD is related to the frequency distribution of the profile, while the area under the PSD is related to the RMS (squared) of the random profile. It has been assumed that the profiles, which are generated with a frequency of 1000 Hz, have RMS between 1 and 4 mm.

A random burr profile using a PSD slope of -2 and a RMS of 2.5 mm and the related simulation results are presented in Figure 15. It can be noticed that the proposed mechanism performs well also for a generic burr profile. In particular, the compliance of the mechanism is exploited to reduce the cutting forces and, as a consequence, a second cutting cycle is necessary to completely remove the burr (see Figure 16). Similarly to the Test case 5 (Section 5.3.5) small bounces on the mechanical stop are visible in the middle plot of both Figure 15; Figure 16 (for example after $t = 0.55$ s, after $t = 1.9$ s, etc.). From the analysis of Figure 16, it can be noticed that after the second cutting cycle a very high precision is ensured: most of the burr profile is at 2.85×10^{-4} mm that is the equilibrium position of the mechanical stop, and very small variations ($< 1 \times 10^{-5}$ m) with respect to this value are present. Indeed, in the second cutting cycle the grinding wheel support is always in contact with the mechanical stop, and the small variations in the burr profile are due to the (low) compliance of the mechanical stop. In this case the compliance of the mechanism is not exploited, since the maximum burr height is below 2.5 mm, which is the minimum burr height that is necessary to make the mechanism work in the compliant mode, as explained in Section 5.3. Very similar conclusions can be drawn when other values of PSD slope and RMS are used (as above specified).

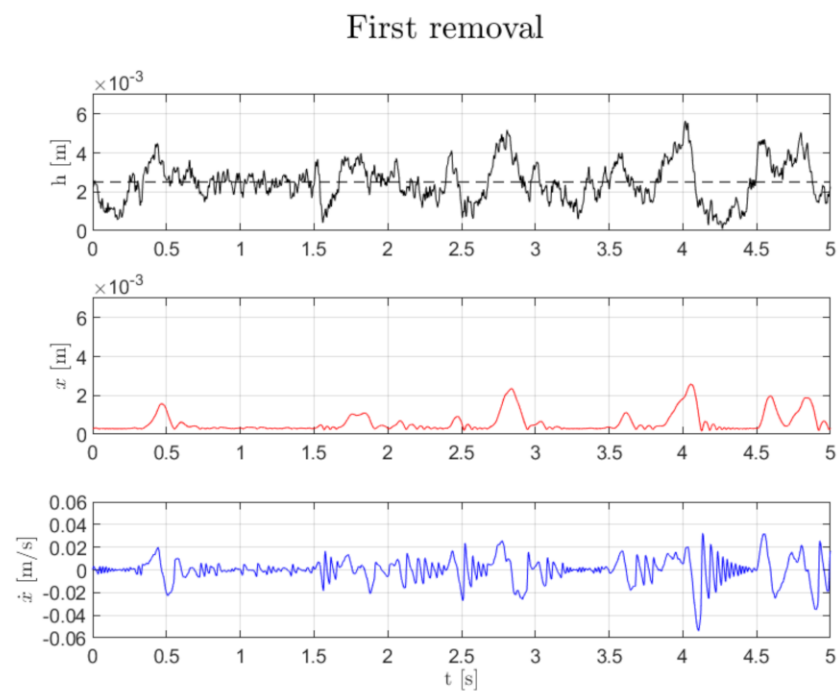


Figure 15. Generic burr profile, first cutting cycle (**top**); position (**middle**) and velocity (**bottom**) of the grinding wheel support.

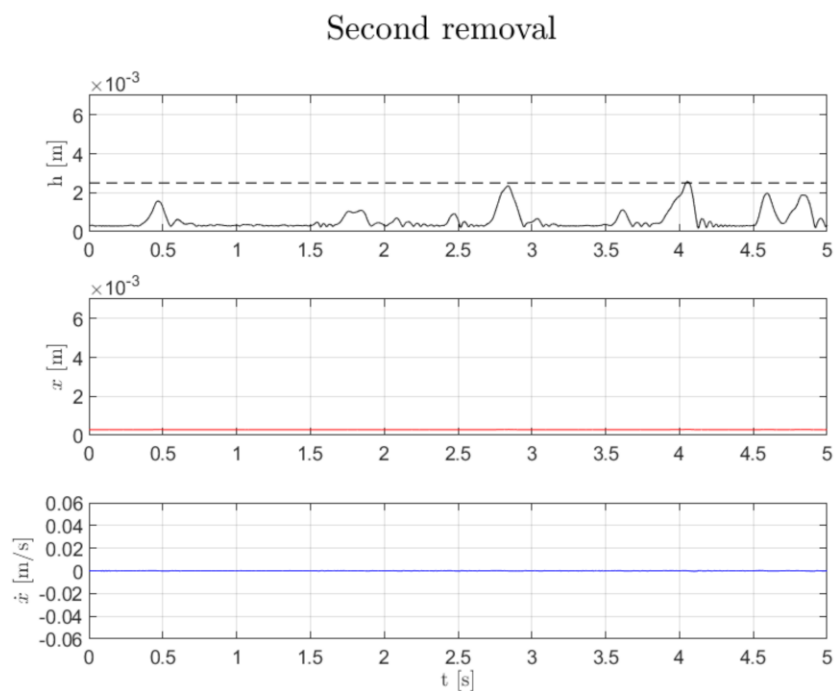


Figure 16. Generic burr profile, second cutting cycle (**top**); position (**middle**) and velocity (**bottom**) of the grinding wheel support. Please notice that the scale of these graphs are the same of Figure 15 for comparison purposes.

6. Conclusions

A mechanism has been designed to be used in robotic deburring to ensure a precision cut and to reduce cutting forces and avoid breaks of the robot/spindle in the case of high and irregular burr profiles. The mechanism is based on a classic slider-crank, which is provided with springs in order to give the desired force-displacement response. In the event that the burr is too high, it exploits its compliance to reduce the cutting forces automatically,

and is able to return to the baseline configuration when the burr thickness is acceptable again. After the specification of the desired stiffness curve, the main design parameters of the system have been derived thanks to an optimization method. The effectiveness of the proposed mechanism is verified by means of dynamic simulations using selected test cases. The simulations showed that, when the compliance of the mechanism is exploited to reduce the cutting forces, a second cutting cycle is necessary to completely remove the burr and ensure a high cutting precision. With the dataset considered, the (normal) deburring forces remain always below 150 N thanks to the design of the mechanism, even if the burr height would generate nominal forces much larger. This has been shown both with basic profiles, such as steps, and with more realistic random profiles, thus ensuring cutting without the risk of damaging the cutting tool. A limitation of the present work is the fact that the proposed system needs to be validated experimentally, paying particular attention to the vibrations induced due to the cutting operation, which could make it necessary to improve the design. The experimental validation of the proposed mechanism and the development of a dynamic model that includes the manipulator model will be part of future work.

Author Contributions: Conceptualization, M.B., S.C. and M.M.; methodology, M.B., S.C. and M.M.; software, M.B.; formal analysis, M.B.; investigation, M.B., S.C. and M.M.; writing—original draft preparation, M.B. and S.C.; writing—review and editing, S.C. and M.M.; supervision, S.C. and M.M. All authors have read and agreed to the published version of the manuscript.

Funding: This research received no external funding.

Institutional Review Board Statement: Not applicable.

Informed Consent Statement: Not applicable.

Data Availability Statement: Not applicable.

Conflicts of Interest: The authors declare no conflict of interest.

References

1. Onstein, I.F.; Semeniuta, O.; Bjerken, M. Deburring Using Robot Manipulators: A Review. In Proceedings of the 3rd International Symposium on Small-scale Intelligent Manufacturing Systems (SIMS), Gjøvik, Norway, 10–12 June 2020.
2. Brunete, A.; Gambao, E.; Koskinen, J.; Heikkilä, T.; Kaldestad, K.B.; Tyapin, I.; Hovland, G.; Surdilovic, D.; Hernando, M.; Bottero, A.; et al. Hard material small-batch industrial machining robot. *Robot. Comput. Integr. Manuf.* **2018**, *54*, 185–199. [\[CrossRef\]](#)
3. Pan, Z.; Zhang, H.; Zhu, Z.; Wang, J. Chatter analysis of robotic machining process. *J. Mater. Process. Technol.* **2006**, *173*, 301–309. [\[CrossRef\]](#)
4. Cordes, M.; Hintze, W.; Altintas, Y. Chatter stability in robotic milling. *Robot. Comput. Integr. Manuf.* **2019**, *55*, 11–18. [\[CrossRef\]](#)
5. Gillespie, L.K. *Deburring and Edge Finishing Handbook*; Society of Manufacturing Engineers: Southfield, MI, USA, 1999.
6. Li, W.; Wang, Y.; Fan, S.; Xu, J. Wear of diamond grinding wheels and material removal rate of silicon nitrides under different machining conditions. *Mater. Lett.* **2007**, *61*, 54–58. [\[CrossRef\]](#)
7. Gillespie, L.K. Deburring precision miniature parts. *Precis. Eng.* **1979**, *1*, 189–198. [\[CrossRef\]](#)
8. Babbar, A.; Jain, V.; Gupta, D. In vivo evaluation of machining forces, torque, and bone quality during skull bone grinding. Proceedings of the Institution of Mechanical Engineers, Part H. *J. Eng. Med.* **2020**, *234*, 626–638. [\[CrossRef\]](#) [\[PubMed\]](#)
9. Babbar, A.; Jain, V.; Gupta, D.; Agrawal, D.; Prakash, C.; Singh, S.; Wu, L.Y.; Zheng, H.Y.; Królczyk, G.; Bogdan-Chudy, M. Experimental analysis of Wear and Multi-Shape Burr Loading during Neurosurgical Bone Grinding. *J. Mater. Res. Technol.* **2021**, *12*, 15–28. [\[CrossRef\]](#)
10. Li, C.; Li, X.; Wu, Y.; Zhang, F.; Huang, H. Deformation mechanism and force modelling of the grinding of YAG single crystals. *Int. J. Mach. Tools Manuf.* **2019**, *143*, 23–37. [\[CrossRef\]](#)
11. Tao, Y.; Zheng, J.; Lin, Y. A sliding mode control-based on a RBF neural network for deburring industry robotic systems. *Int. J. Adv. Robot. Syst.* **2016**, *13*, 8. [\[CrossRef\]](#)
12. Qian, Y.; Yuan, J.; Bao, S.; Gao, L. Sensorless Hybrid Normal-Force Controller with Surface Prediction. In Proceedings of the IEEE International Conference on Robotics and Biomimetics (ROBIO), Yunnan, China, 6–8 December 2019.
13. Pappachan, B.K.; Caesarendra, W.; Tjahjowidodo, T.; Wijaya, T. Frequency domain analysis of sensor data for event classification in real-time robot assisted deburring. *Sensors* **2017**, *17*, 1247. [\[CrossRef\]](#)
14. Kakoi, H.; Yanagihara, K.; Akashi, K.; Tsuchiya, K. Development of Vertical Articulated Robot Deburring System by Using Sensor Feedback. In *IOP Conference Series: Materials Science and Engineering*; IOP: Bristol, UK, 2020.

15. Hu, J.; Kabir, A.M.; Hartford, S.M.; Gupta, S.K.; Pagilla, P.R. Robotic deburring and chamfering of complex geometries in high-mix/low-volume production applications. In Proceedings of the IEEE 16th International Conference on Automation Science and Engineering (CASE), Virtual meeting, 20–21 August 2020.
16. El Naser, Y.H.; Atali, G.; Karayel, D.; Özkan, S.S. Prototyping an Industrial Robot Arm for Deburring in Machining. *Akad. Platf. Mühendislik Fen Bilimleri Derg.* **2020**, *8*, 304–309.
17. Guo, W.; Li, R.; Zhu, Y.; Yang, T.; Qin, R.; Hu, Z. A Robotic Deburring Methodology for Tool Path Planning and Process Parameter Control of a Five-Degree-of-Freedom Robot Manipulator. *Appl. Sci.* **2019**, *9*, 2033. [\[CrossRef\]](#)
18. Lai, C.Y.; Chavez, D.E.V.; Ding, S. Transformable parallel-serial manipulator for robotic machining. *Int. J. Adv. Manuf. Technol.* **2018**, *97*, 2987–2996. [\[CrossRef\]](#)
19. Vuong, N.-D.; Li, R.; Chew, C.-M.; Jafari, A.; Polden, J. A novel variable stiffness mechanism with linear spring characteristic for machining operations. *Robotica* **2017**, *35*, 1627. [\[CrossRef\]](#)
20. Wang, W.; Fu, X.; Li, Y.; Yun, C. Design and implementation of a variable stiffness actuator based on flexible gear rack mechanism. *Robotica* **2018**, *36*, 448–462. [\[CrossRef\]](#)
21. Barrett, E.; Reiling, M.; Barbieri, G.; Fumagalli, M.; Carloni, R. Mechatronic design of a variable stiffness robotic arm. In Proceedings of the IEEE/RSJ International Conference on Intelligent Robots and Systems (IROS), Vancouver, BC, Canada, 24–28 September 2017.
22. Petit, F.; Daasch, A.; Albu-Schäffer, A. Backstepping Control of Variable Stiffness Robots. *IEEE Trans. Control Syst. Technol.* **2015**, *23*, 2195–2202. [\[CrossRef\]](#)
23. Sciavicco, L.; Siciliano, B. *Modelling and Control of Robot Manipulators*; Springer Science & Business Media: Berlin/Heidelberg, Germany, 2012.
24. Doria, A.; Cocuzza, S.; Comand, N.; Bottin, M.; Rossi, A. Analysis of the compliance properties of an industrial robot with the Mozzi axis approach. *Robotics* **2019**, *8*, 80. [\[CrossRef\]](#)
25. Bottin, M.; Cocuzza, S.; Comand, N.; Doria, A. Modeling and identification of an industrial robot with a selective modal approach. *Appl. Sci.* **2020**, *10*, 4619. [\[CrossRef\]](#)
26. Nemec, B.; Yasuda, K.; Ude, A. A Virtual Mechanism Approach for Exploiting Functional Redundancy in Finishing Operations. *IEEE Trans. Autom. Sci. Eng.* **2020**. [\[CrossRef\]](#)
27. Esquivel, E.; Carbone, G.; Ceccarelli, M.; Jáuregui, J.C. A Dynamic Compensation for Roll Hemming Process. *IEEE Access* **2018**, *6*, 18264–18275. [\[CrossRef\]](#)
28. Görgülü, İ.; Carbone, G.; Dede, M.İ.C. Time efficient stiffness model computation for a parallel haptic mechanism via the virtual joint method. *Mech. Mach. Theory* **2020**, *143*, 103614. [\[CrossRef\]](#)
29. Kalpakjian, S. *Manufacturing Processes for Engineering Materials*; Pearson Education India: Tamil Nadu, India, 1984.
30. Malkin, S.; Guo, C. *Grinding Technology: Theory and Application of Machining with Abrasives*; Industrial Press Inc.: New York, NY, USA, 2008.
31. Marinescu, I.D.; Hitchiner, M.P.; Uhlmann, E.; Rowe, W.B.; Inasaki, I. *Handbook of Machining with Grinding Wheels*, 2nd ed.; CRC Press: Boca Raton, FL, USA, 2016.
32. Her, M.G.; Kazerooni, H. Automated robotic deburring of parts using compliance control. *J. Dyn. Sys. Meas. Control.* **1991**, *113*, 60–66. [\[CrossRef\]](#)
33. Shinozuka, M.; Deodatis, G. Simulation of stochastic processes by spectral representation. *Appl. Mech. Rev.* **1991**, *44*, 191–204. [\[CrossRef\]](#)